Multiple scattering effects of MeV electrons in very thick amorphous specimens

ARTICLE *in* ULTRAMICROSCOPY · FEBRUARY 2010

Impact Factor: 2.44 · DOI: 10.1016/j.ultramic.2009.12.013 · Source: PubMed

Fang Wang
Xi'an Jiaotong University

Meng Cao
Xi'an Jiaotong University

Akio Takaoka
Osaka University

Ultramicroscopy 110 (2010) 259–268

Contents lists available at ScienceDirect

Ultramicroscopy

journal homepage: www.elsevier.com/locate/ultramic

Multiple scattering effects of MeV electrons in very thick amorphous specimens

Fang Wang [a], Hai-Bo Zhang [a,*], Meng Cao [a], Ryuji Nishi [b], Akio Takaoka [b]

[a] Key Laboratory for Physical Electronics and Devices of the Ministry of Education, Department of Electronic Science and Technology, Xi'an Jiaotong University, Xi'an 710049, People's Republic of China

[b] Research Center for Ultrahigh Voltage Electron Microscopy, Osaka University, 7-1 Mihogaoka, Ibaraki, Osaka 567-0047, Japan

ARTICLE INFO

Article history:
Received 30 March 2009
Received in revised form
8 December 2009
Accepted 22 December 2009

Keywords:
Multiple scattering
High-energy electrons
Thick specimens
Transmission electron microscopy

ABSTRACT

Multiple scattering has an important influence on the analysis of microns-thick specimens with MeV electrons. In this paper, we report on effects of multiple scattering of MeV electrons on electron transmission and imaging of tilted and thick amorphous film specimens by experiment and theoretical analysis. Electron transmission for microns-thick epoxy-resin and SiO_2 specimens calculated by the multiple elastic-scattering theory is in good agreement with measurements in the ultrahigh voltage electron microscope (ultra-HVEM) at Osaka University. Electron transmission and electron energy are then presented in an approximate power law. The bright-field ultra-HVEM images of gold particles on the top or bottom surfaces of 5 and 15 μm thick specimens further illustrate the effect of multiple scattering on image quality. The observed top-bottom effect for the very thick specimens appears to be mainly caused by multiple elastic scattering. With increase in the accelerating voltage from 1 to 2 MV, image blurring, contrast, the signal-to-noise ratio, and the top-bottom effect are improved because of reduction in the influence of multiple scattering. However, the effect of specimen thickness on image blurring is shown to be stronger than that of accelerating voltage. At the 2 MV accelerating voltage, the 100 nm gold particle can be imaged with less blurring of ~4 nm when located at the bottom surface of a 15 μm thick epoxy-resin specimen.

1. Introduction

As a well-known physical phenomenon, multiple scattering of electrons with atoms has been influencing the analysis of a relatively thick specimen in transmission electron microscopy (TEM) [1–7]. Here, incident electrons may be multiply scattered while penetrating through the specimen whose thickness is much larger than the mean free path of electrons, resulting in the spread of angular and spatial distributions, and energy loss of transmitted electrons. Multiple scattering in thick specimens will therefore change the property of electron transmission and degrade the image quality [4,7–9]. In addition, the top-bottom effect may be presented in the TEM mode due to multiple scattering, in which objects near the bottom of the specimen can be imaged with better image quality than those near the top [10]. Consequently, multiple scattering restricts the further application of TEM in thick specimens. Especially, in electron tomography, tilting a specimen with large angles will increase its effective thickness, for instance, the effective thickness almost triples at 70° tilt. This makes multiple scattering remarkable, resulting in blurring of projection images and the quality deterioration in electron tomography [11–19]. The significance of multiple scattering depends on the specimen property and the incident electron energy. Recently, there is an increasing need for the observation of very thick specimens. For example, a bulk specimen of the semiconductor device containing multilayer structures and a specimen of biological structures may be several microns thick [8,11–13,20].

Hence, utilization of the high voltage electron microscope (HVEM) [21], especially the ultra-HVEM with the MV accelerating voltage [22–24], has been a practical and effective approach for analysis and electron tomography of thick specimens for the reduction in electron scattering events[11,19,25–31]. As an alternative for observing thick specimens, the scanning transmission electron microscope (STEM) is free of chromatic aberration of the objective lens [5]. Different from most STEMs in which the probe convergence semi-angle is as large as ~10 mrad [32,33], a few STEMs, e.g., the scanning confocal electron microscope and the STEM using the probe beam with a very small convergence angle, can produce better image quality for thick specimens than the conventional TEM [34,35], but there is still occurrence of multiple scattering of electrons.

* Corresponding author: Tel.: +86 29 8266 4963; fax: 86 29 8266 4974
E-mail address: hbzhang@mail.xjtu.edu.cn (H.-B. Zhang).

0304-3991/$ - see front matter © 2009 Elsevier B.V. All rights reserved.
doi:10.1016/j.ultramic.2009.12.013

There has been a lot of research on elastic scattering of electrons of the primary energy less than 300 keV and its influence on electron transmission for thin specimens with typical thicknesses less than the mean free path of electrons, e.g., 200 nm [36–38]. Some investigations on scattering of 1.2–3 MeV electrons in much thicker simple substances such as Al and Au were reported [39,40]. Recently, multiple elastic scattering in microns-thick specimens and the consequential electron transmission or imaging characteristics have been reviewed for the STEM at the accelerating voltage from several kV to 300 kV [9,13–15,33,41,42]. Because resolution in STEM is determined by the probe size, the objects near the bottom of the specimen are blurred more than those near the top due to beam broadening [33,42].

However, there is still need for further investigations regarding multiple scattering effects of MeV electrons on electron transmission and imaging for microns-thick amorphous compound specimens by experimental and theoretical analysis, though a limited number of related researches have been reported. In the previous work, we have shown that multiple elastic scattering in thick specimens is an important factor for the variation of electron transmission [7]. The intensity of transmitted electrons for thick specimens including the background of lighter materials in the bright-field mode will decay with the increase of specimen thickness [7,43]. Especially, the background brightness will decrease due to the increased loss of elastically scattered electrons at the objective aperture to form amplitude contrast. This may in turn degrade amplitude contrast and the signal-to-noise ratio of the image for thick specimens. Nevertheless, an investigation has yet to be provided to understand the influence of specimen property and electron energy on electron transmission in the multiple scattering process of MeV electrons. On the other hand, both multiple elastic scattering and chromatic aberration resulting from inelastic scattering in a specimen may increase with the increase of specimen thickness, so resolution and image contrast may be deteriorated [4,12]. Here, imaging properties of crystal specimens in the ultra-HVEM have been examined [31,44], but for microns-thick amorphous specimens there is lack of report on the effect of increasing the accelerating voltage of electrons in the range of MV in improving the image quality. Moreover, the top-bottom effect reported for the conventional TEM [10,45–47] has also been observed for thick amorphous specimens with the ultra-HVEM in our previous work [48]. The variation of the top-bottom effect with the MV accelerating voltage in the ultra-HVEM has not been reported, and the influence of multiple elastic and inelastic scattering on image blurring of objects on the top or bottom surface is still unclear. Compared with STEM, the advantage of the ultra-HVEM on the observation of microns-thick specimens should be evaluated. Furthermore, the observation or electron tomography of large-scale structures in microns-thick specimens in biology and materials science requires the experimental and theoretical analysis on electron transmission and imaging properties for thick specimens.

The aim of the present work, therefore, is to give a comprehensive investigation for multiple scattering effects of MeV electrons in microns-thick amorphous specimens under different conditions of specimen and electron energy. We have measured electron transmission and imaging characteristics with the ultra-HVEM [24] developed at Osaka University whose highest accelerating voltage of 3 MV is also the world's highest among electron microscopes. In addition, although the well-developed multiple scattering theory cannot be directly applied to the imaging process of transmission electrons, we have analyzed experimental results from the existing multiple scattering theory. In this paper, we first introduce the theoretical consideration related to multiple scattering effects. By conducting experiments at MV accelerating voltages of electrons, both electron transmission for tilted epoxy-resin and SiO_2 specimens of microns-thick and bright-field ultra-HVEM images of nanometer gold particles on surfaces of thick epoxy-resin specimens are then presented. Here, in order to research the thickness dependence of electron transmission conveniently, specimens are tilted to a series of angles to obtain different effective thicknesses on the direction of incident electrons [49]. Variations of electron transmission with the MV accelerating voltage of electrons, the effective thickness, and the specimen material are also compared with the calculations based on the theory of multiple elastic scattering. Image blurring and the top-bottom effect of the microns-thick specimens, observed in the ultra-HVEM, are also analyzed from the point of view of multiple scattering to evaluate the influence of the MV accelerating voltage in improving image quality.

2. Theoretical considerations

2.1. Single and multiple scattering

We begin by introducing some fundamentals related to multiple scattering of MeV electrons in thick specimens. The interactions between electrons and specimen atoms include elastic and inelastic scattering. In the elastic scattering process, incident electrons are diffracted in the Coulomb potential of the atomic nucleus without energy loss. Most contribution to the total elastic cross-section for fast electrons is from the small-angle scattering. The total elastic cross-section with the relativistic correction and small-angle approximation is given by the integral of the elastic differential cross-section $d\sigma_{el}/d\Omega$ over all scattering angles as [5]

$$\sigma_{el} = \int_0^{\pi} \frac{d\sigma_{el}}{d\Omega} 2\pi \sin\theta \, d\theta = \frac{Z^2 R^2 \lambda'^2 (1+E/E_0)^2}{\pi a_H^2} \tag{1}$$

where Z is the atomic number, the screening radius $R=a_H/Z^{1/3}$, the Bohr radius $a_H=5.29\times10^{-11}$ m, E the incident electron energy in keV, $E_0=511$ keV, and λ' the wavelength of electrons. The partial elastic cross-section for electrons scattered through angles larger than θ is

$$\sigma_{el}(\theta) = \int_{\theta}^{\pi} \frac{d\sigma_{el}}{d\Omega} 2\pi \sin\theta \, d\theta = \sigma_{el} \frac{1}{1+(\theta/\theta_0)^2} \tag{2}$$

where $\theta_0=\lambda'/2\pi R$ is the characteristic scattering angle at which the scattering amplitude falls to its half value. The elastic mean free path of electrons is $\lambda_{el}=A/(N_A\rho\sigma_{el})$, where A denotes the atomic weight, N_A the Avogadro number, and ρ the specimen density. On the other hand, inelastic scattering is the interaction between incident electrons and atomic electrons with the energy loss of incident electrons by various inelastic processes but less change of the moving direction than elastic scattering. The inelastic cross-section for electrons scattered through angles larger than θ is given by [5]

$$\sigma_{inel}(\theta) = \frac{4ZR^2\lambda'^2(1+E/E_0)^2}{\pi a_H^2} \left[\frac{-1}{4\left[1+(\theta/\theta_0)^2\right]} + \ln\sqrt{1+(\theta/\theta_0)^2} \right] \tag{3}$$

Fig. 1 shows variations of $\sigma_{el}(\theta)$ and $\sigma_{inel}(\theta)$ of 3 MeV electrons with the scattering angle θ for epoxy-resin and SiO_2, which were calculated using Eqs. (2) and (3). Here, for compound materials, the average atomic number $\overline{Z}$ and atomic weight $\overline{A}$ can be used to simplify the calculation [50]. For epoxy-resin $[C_{11}H_{12}O_3]_n$, the parameters are taken as $\overline{Z}=6.19$, $\overline{A}=12.31$, and $\rho=1.25$ g/cm^3. For SiO_2, these parameters become $\overline{Z}=10$, $\overline{A}=20$, and $\rho=2.6$ g/cm^3. As shown in Fig. 1, the cross-sections decrease with the

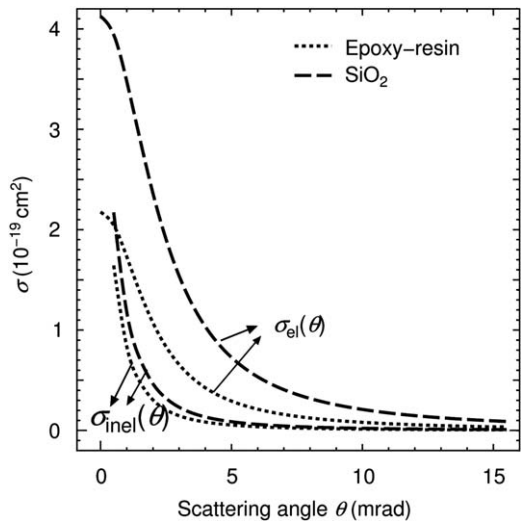

Fig. 1. Calculated elastic and inelastic cross-sections $\sigma_{el}(\theta)$ and $\sigma_{inel}(\theta)$ as a function of the scattering angle θ. The electron energy is 3 MeV, and the specimens are epoxy-resin and SiO_2.

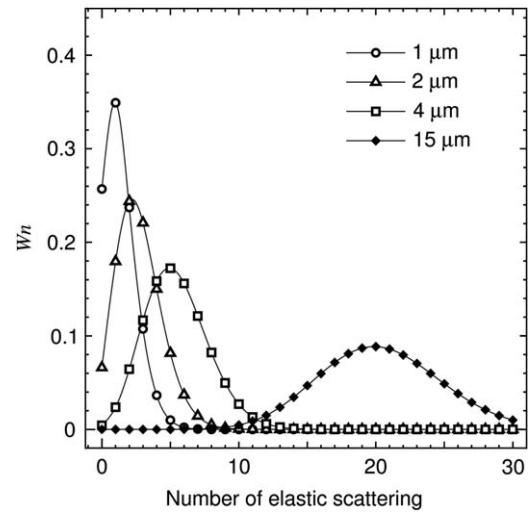

Fig. 2. Calculated probability distributions W_n of n times elastic scattering for a 2 MeV electron penetrating through 1–15 μm thick epoxy-resin specimens. The incident electrons may be scattered elastically more times with the increase of specimen thickness.

increase of θ, and $\sigma_{inel}(\theta)$ decreases more rapidly. The ratio of elastic to inelastic cross-sections increases with the increase of atomic weight of the specimen [5], so it is higher for SiO_2 of higher atomic weight than for epoxy-resin. For MeV electrons, $\sigma_{inel}(\theta)$ appears to have lower values and is more concentrated in small angles than $\sigma_{el}(\theta)$. The characteristic angle θ_0 of elastic scattering in Eq. (2) for 3 MeV electrons and epoxy-resin can be calculated as 1.9 mrad, whereas the characteristic angle of inelastic scattering responsible for the decrease of the inelastic differential cross-section $d\sigma_{inel}/d\Omega$ with the increase of θ may be one or two orders of magnitude smaller than θ_0 [5,36]. Accordingly, the angular deflection of inelastic scattering of MeV electrons is so small that the energy loss of incident electrons should be the main result of inelastic scattering.

For multiple scattering, the probability W_n of n times elastic scattering for an electron through a specimen of the thickness H along the incident direction is approximated as Poisson distribution [51]

$$W_n = \frac{(H/\lambda_{el})^n}{n!}\exp(-H/\lambda_{el}) \tag{4}$$

Fig. 2 shows the Poisson distributions of the number of elastic-scattering events calculated according to Eq. (4) for 2 MeV electrons penetrating through epoxy-resin specimens of different thicknesses. It should be noted that the real distribution is discrete. When the specimen thickness increases to 15 μm, the number of elastic-scattering events distributes to a larger range and becomes more smooth and symmetric. Nearly all transmitted electrons will be multiply scattered. The average elastic-scattering number can be calculated as $n_{el}=H/\lambda_{el}$. Here, n_{el} is proportional to the specimen thickness H. However, for a given specimen, the dependence of n_{el} on the electron energy E is $n_{el} \propto [1-(1+E/E_0)^{-2}]^{-1}$. The decrease of n_{el} in microns-thick specimens will be slight with the increase of electron energy in the range of MeV, while the scattering angle of single elastic scattering may decrease considerably. Therefore, higher electron energy is more advantageous in reducing the scattering angle rather than the scattering event.

2.2. Multiple elastic scattering and electron transmission

The increase of the elastic-scattering events in thick specimens is likely to induce the angular distribution of transmitted electrons by multiple elastic scattering, and the effect on electron transmission can be estimated by theoretical methods. Characteristics of transmitted electrons multiply scattered in a solid can be obtained by various methods such as the multiple-scattering integral, the solution of the Boltzmann transport equation or the Monte-Carlo simulation at the expense of complicated calculations [5,52,53]. Based on the error theory, the multiple elastic scattering theory by Bothe has a simple analytic solution to describe the angular distribution of transmitted electrons as a two-dimensional Gaussian distribution. Bothe's theory neglects large-angle single scattering and energy loss, assuming that the successive scatterings are independent [3]. The angular distribution $f(H,\theta)$ of transmitted electrons with the angle θ from the incident direction exiting from the specimen of the thickness H is described in a Gaussian form [5]

$$f(H,\theta) \propto \exp(-\theta^2/\overline{\theta}^2) \tag{5}$$

with $\overline{\theta}$ as

$$\overline{\theta} = 1.82\times 10^5 \left(\frac{\rho}{A}\right)^{1/2} \frac{Z}{E}\frac{1+E/E_0}{1+E/2E_0} H^{1/2} \tag{6}$$

where E is in eV and H is in cm. The angular distribution will spread widely with the increase of specimen thickness, especially in the multiple elastic-scattering regime, and become more concentrated at a higher electron energy.

Furthermore, the variation of the angular distribution of transmitted electrons will affect the imaging signal intensity. In the bright-field TEM mode, electron scattered within the half angle α_0 of the objective aperture can be collected as the transmission signal for imaging. Inelastic scattering of MeV electrons distributes mostly in much smaller angles compared with a half angle α_0 of ~2 mrad in the ultra-HVEM. In addition, the elastic cross-sections will have little variations because the rate of continuous energy loss of electrons due to inelastic scattering is inconsiderable as about 0.2 and 0.4 keV/μm for MeV electrons penetrating the microns-thick epoxy-resin and SiO_2 specimens [54], respectively. Therefore, the normalized electron transmission I_t/I_0 can be estimated by the multiple elastic-scattering theory, neglecting the inelastic scattering effect as a source of the background signal. Here, I_t is the intensity of electrons penetrating through a specimen, and I_0 is the intensity of incident electrons [7]. Accordingly, I_t/I_0 can be derived by the

integral of the angular distribution $f(H,\theta)$ over α_0 and the approximation $\sin\theta \approx \theta$ as

$$\begin{aligned} I_t/I_0 &= \int_0^{\alpha_0} \exp(-\theta^2/\overline{\theta}^2)\sin\theta\,d\theta / \int_0^{\pi} \exp(-\theta^2/\overline{\theta}^2)\sin\theta\,d\theta \\ &\approx \left[1-\exp(-\alpha_0{}^2/\overline{\theta}^2)\right] / \left[1-\exp(-\pi^2/\overline{\theta}^2)\right] \\ &\approx 1-\exp(-\alpha_0{}^2/\overline{\theta}^2) \end{aligned} \tag{7}$$

where the factor $1-\exp(-\pi^2/\overline{\theta}^2)$ can be dropped due to the small value of $\overline{\theta}$. In addition, as shown in Fig. 2, with the increase of the thickness of epoxy-resin, the majority of scattering is not single elastic scattering, but rather multiple elastic scattering. Therefore, using Bothe's angular distribution, which underestimates the large-angle single elastic scattering, will have little effect on the calculation of electron transmission, especially for very thick specimens.

2.3. Effects of multiple scattering on imaging

Multiple elastic and inelastic scattering may result in the deterioration of TEM images for thick specimens by different mechanisms. Multiple elastic scattering in thick specimens may cause the spatial broadening of transmitted electrons. The spatial broadening in the amorphous specimen can be evaluated in terms of x_0, which represents the lateral spreading of most electrons from the incident axis while passing through the specimen of the thickness H. The expression of x_0 with the relativistic correction can be [5]

$$x_0 = 1.05 \times 10^5 \left(\frac{\rho}{A}\right)^{1/2} \frac{Z}{E} \frac{1+E/E_0}{1+E/2E_0} H^{3/2} \tag{8}$$

where E is in eV, and x_0 and H are in cm. The value of x_0 depends on the specimen property and electron energy. More importantly, the wide spatial broadening in a thick specimen may disturb image information formed by amplitude contrast in TEM for objects near the top of the specimen.

The angular dispersion of electrons due to multiple elastic scattering may also produce some image blurring. When arriving at objects near the bottom of the thick specimen, electrons have been scattered in different directions although they enter the specimen as an approximate parallel beam at first. As shown in Fig. 3, electrons with large angles in dot and dot-dash lines before scattered by objects may form extra images superposed on the image formed by electrons with normal incident direction in solid lines, causing a blurring disc in the focal plane and the resultant image quality degradation. The wider the angular dispersion, the larger the blurring disc.

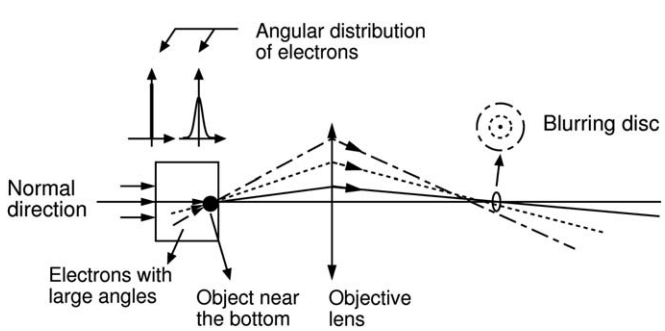

Fig. 3. Schematic of the image blurring formation due to the angular dispersion of electrons before being scattered with an object near the bottom of the specimen. The solid paths represent electrons incident on the thick specimen and the object in the normal direction successively. The dot and dot-dash paths show electrons multiply scattered in the thick specimen with different angles, respectively, before being scattered with the object inside. Angular distributions of electrons before and after being multiply scattered with the specimen are illustrated. A blurring disc may thus form in the focal plane. The wider angular dispersion causes the larger blurring disc.

Multiple inelastic scattering may occur in thick specimens and cause chromatic aberration of images although inelastic scattering may be minor compared with elastic scattering for MeV electrons. The energy distribution of electrons can be broadened by multiple inelastic scattering. As the full width at half height of the energy distribution, ΔE is usually estimated by the Landau model as [55]

$$\Delta E = \frac{61.2 \times 10^4 \rho H}{(v/c)^2} \frac{Z}{A} \tag{9}$$

where v/c is the electron velocity in units of the velocity of light, H is in cm, and ΔE is in eV. ΔE decreases with the increase of electron energy and increases proportionally to the specimen thickness H. The point-to-point resolution r_c defined from the blurring disc of chromatic aberration is expressed with the relativistic correction by [55]

$$r_c = C_c \alpha_0 \frac{\Delta E}{2E} \frac{1+E/E_0}{1+E/2E_0} \tag{10}$$

where C_c is the chromatic aberration coefficient. By increasing electron energy, chromatic aberration is thus reduced. Note that in TEM images, chromatic aberration affects images of objects near the top and bottom of the specimen equivalently [2]. However, the effects of the spatial broadening and the angular distribution of electrons may depend on the position of objects in the thick specimen. For example, the greater distance between objects and the bottom surface of the specimen should lead to more deterioration of image quality due to the spatial broadening.

3. Experimental method

The ultra-HVEM [24] was used for measurement of electron transmission and acquirement of TEM images of thick specimens under various experimental conditions. Electron transmission was measured with the previously reported method [7] as illustrated in Fig. 4. The beam goes down in space. The specimens were tilted epoxy-resin and SiO_2 films with the original thickness h of 1–5 μm. By tilting the specimen to a series of angles β with a 360°-tilt holder [49], the effective thickness H of the specimen along the direction of incident electrons increases as $h/\cos\beta$. The diameter of the objective aperture used in the experiment was 70 μm and the corresponding half angle α_0 was 2.92 mrad. The signal intensity I_t and I_0 of electrons, in the presence and absence of the specimen, were collected by the Faraday cup in the bright-field TEM mode. Hence, variations of the normalized electron transmission I_t/I_0 with the effective thickness of tilted specimens and the accelerating voltage can be measured successively.

Ultra-HVEM images in amplitude contrast of gold particles on surfaces of thick specimens were obtained to present effects of multiple scattering on image quality. The specimens were 15 and 5 μm thick epoxy-resin films with colloidal gold particles originally on the top surfaces. The diameter of gold particles is 100 nm with the deviation below 4%. By tilting the specimen to 180° by means of the 360°-tilt holder, gold particles turned to the bottom of the specimen. Images of gold particles on the top and bottom surfaces of the specimens were recorded successively by a high-performance cooled charge-coupled device (CCD) camera at the accelerating voltage of 1 and 2 MV. The half angle α_0 was adjusted to 2.08 mrad. In order to enhance the brightness of images at 1 MV or images of the 15 μm thick specimen, the emission current of the electron gun was increased.

In the experimental operation, it is important to confirm the position of gold particles on the specimen because an error may

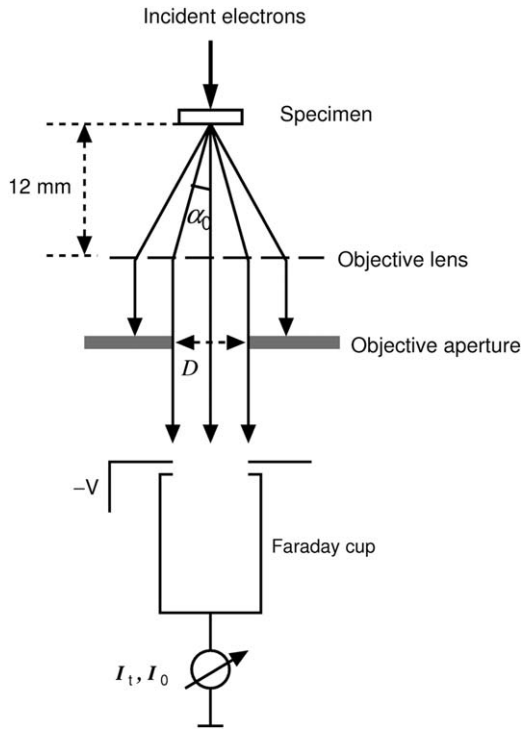

Fig. 4. Schematic of electron transmission and experimental set up in the ultra-HVEM. α_0 and D represent, respectively, the half angle and the diameter of the objective aperture. In the measurement of electron transmission, D is fixed at 70 μm. The focal length of the objective lens is 12 mm and therefore α_0 is 2.92 mrad. I_t and I_0 is the intensity of electrons collected in the presence and absence of a specimen, respectively [7].

unexpectedly occur by placing the specimen upside down or the leakage of gold particles from one side of the specimen to the other side. We thus verified the position of gold particles observed in the ultra-HVEM experiment to be on the right side of the specimen from their scanning electron microscopic images that are formed by secondary electrons emitted only from the top surface of the specimen.

In addition, the real size of the 100 nm gold particles has been verified by two methods. One was by the scanning electron microscopic images because their image quality is independent of the specimen thickness, and then free of multiple scattering effects. The other was by the ultra-HVEM image of the un-tilted 5 μm specimen at 3 MV with the best image quality or least multiple scattering effects in our experiment. Then the particles' size can be measured by the calibration of these CCD images accurately. On the other hand, using gold particles as large as 100 nm, we could measure image blurring more accurately based on their relatively larger original size. Additionally, larger gold particles could be observed under the low magnification, and they were more stable than smaller gold particles for the less radiation damage caused by electron beam as well as the smaller displacement. Therefore, in our work, we took 100 nm gold particles as objects of imaging to investigate conveniently multiple scattering effects on image quality of thick specimens, rather than smaller gold particles usually used as the labels.

Some additional aspects in experiments should be cautioned. In order to reduce specimen thinning and dimensional changes of gold particles, which result from electron-beam irradiation, we adopted measures as follows. A low magnification of 3000 × was used to prevent strong focusing while measuring the signal intensity of transmitted electrons. Moreover, besides applying protective coatings over the specimens, electron-beam irradiation time for the whole experiments was minimized to decrease the radiation damage to specimens and gold particles. Here, ultra-HVEM images of gold particles located on thick specimens before and after electron-beam irradiation were compared. Little difference in image quality was observed, indicating the radiation damage to be inconsiderable in the experiment of acquiring images of thick specimens.

4. Experimental results

4.1. Electron transmission

Fig. 5 summarizes the measured electron transmission I_t/I_0 as a function of the effective thickness of the tilted epoxy-resin and SiO_2 specimens in symbols at the accelerating voltage of 2 MV. The calculation results of electron transmission according to Eq. (7) based on multiple elastic scattering are plotted in lines. Obviously, I_t/I_0 decays with the increase of H. A stronger scattering effect is shown for SiO_2 due to its heavier average atomic weight, i.e., I_t/I_0 decays more rapidly with the increase of H. For a small thickness, $\log(I_t/I_0)$ decays linearly with H. However, this linear range for epoxy-resin is extended to ~4 μm, at which the average elastic-scattering number n_{el} of transmitted electrons reaches ~6. We consider here that multiple elastic scattering becomes the majority of scattering events.

The measurement results of variations of I_t/I_0 with the accelerating voltage of electrons and corresponding calculation results according to Eq. (7) are further plotted in symbols and a line, respectively, in Fig. 6. The specimen is a 70° tilted 5 μm thick epoxy-resin film with the effective thickness of 14.6 μm. The results show that the higher accelerating voltage leads to higher electron transmission. The measurement value of I_t/I_0 at 3 MV is 7.2 times of that at 1 MV because of the reduction in the multiple elastic-scattering effect. From calculation results, it can be presumed that there exists the approximation $I_t/I_0 \propto E^k$ from 0.5 to 3 MV, where E is in keV, k depends on the specimen material and $k \approx 1.66$ for epoxy-resin in the experiment. Furthermore, the measurement results fit well to this power law.

The consistence of measurements and calculations of I_t/I_0 in Figs. 5 and 6 also indicates that the variation of electron

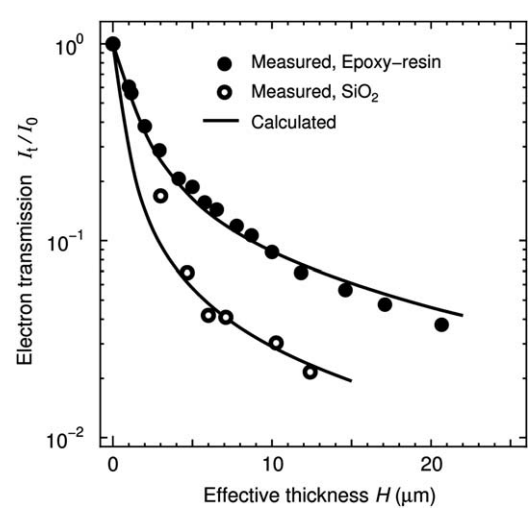

Fig. 5. Measured and calculated electron transmission I_t/I_0 as a function of the effective thickness H of the tilted specimens of epoxy-resin and SiO_2 at the accelerating voltage of 2 MV. The half angle α_0 of the objective aperture is adjusted to 2.92 mrad. I_t/I_0 decays with the increase of H. The linear attenuation range for epoxy-resin is ~4 μm. For SiO_2 I_t/I_0 decays more rapidly due to the heavier average atomic weight.

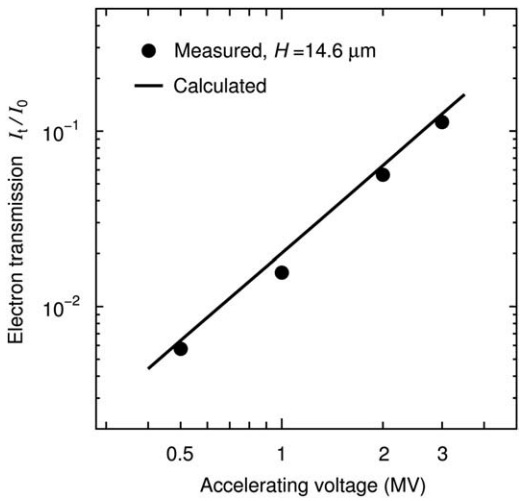

Fig. 6. Measured and calculated values of electron transmission I_t/I_0 vs. the accelerating voltage of electrons. The specimen is a 70° tilted 5 μm thick epoxy-resin film with the effective thickness of 14.6 μm. The half angle α_0 of the objective aperture is 2.92 mrad. I_t/I_0 increases with the increase of accelerating voltage from 0.5 to 3 MV, following an approximate rule as $I_t/I_0 \propto E^{1.66}$. I_t/I_0 at 3 MV is 7.2 times larger than that at 1 MV.

transmission is mainly produced by multiple elastic scattering although electrons may be scattered elastically and inelastically. Therefore, in the case of the MV accelerating voltage and the relatively large objective aperture, it will be reasonable to use the elastic-scattering theory to estimate electron transmission. Note that the possible error of calculations may be from the neglect of inelastic scattering in thick specimens, or the little amount of specimen thinning due to electron beam irradiation.

4.2. Image blurring

Fig. 7 presents ultra-HVEM images of 100 nm gold particles in amplitude contrast at the accelerating voltage of 1 and 2 MV. In Fig. 7a and b, the same gold particles are respectively on the top and bottom surface of a 15 μm thick epoxy-resin specimen at 2 MV. The image quality for the gold particles on the top of the thick specimen is degraded notably. However, the image of the gold particles on the bottom is much clearer. Here, an obvious top-bottom effect is exhibited. Fig. 7c and d show gold-particle images of the 15 μm thick specimen at 1 MV, which have worse image quality than Fig. 7a and b. With the decrease of accelerating voltage, the image of the gold particles on the top of the specimen is blurred more significantly, and the top-bottom effect is aggravated. In Fig. 7, if images at 1 MV had been taken without the adjustment of emission current, they would have been much darker than those at 2 MV due to the lower electron transmission.

Fig. 8 shows images of the gold particles on the top and bottom of a 5 μm thick epoxy-resin specimen at 2 MV. The images are both clear and have little difference in quality. The image contrast and brightness are also higher than those in Fig. 7a and b for the 15 μm thick specimen. Here, with the decrease of specimen thickness, the image quality is improved and the top-bottom effect is then not prominent.

Line profiles of the normalized gray level along the diameter direction of a gold particle are depicted in Fig. 9 to evaluate the deterioration of gold-particle images. The gold particle most close to 100 nm in a clear image is chosen to decrease errors resulting from its size deviation. The apparent diameter d as the central dark region from the gold-particle image is measured by the full width at tenth maximum. Here, image blurring can be obtained as ($d-100$ nm). By comparing line profiles for a gold particle on the

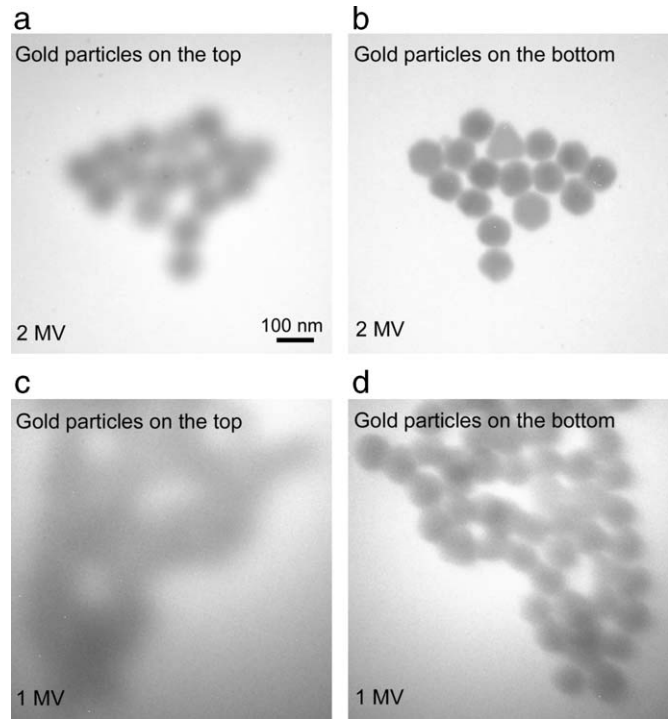

Fig. 7. Bright-field ultra-HVEM images of 100 nm gold particles on the top and bottom surfaces of the 15 μm thick epoxy-resin specimens at the accelerating voltage of : (a), (b) 2 MV and (c), (d) 1 MV. The magnification is 20 000 × and the half angle α_0 of the objective aperture 2.08 mrad. In the experiment, the same areas on the top and bottom of specimens were chosen to be imaged.

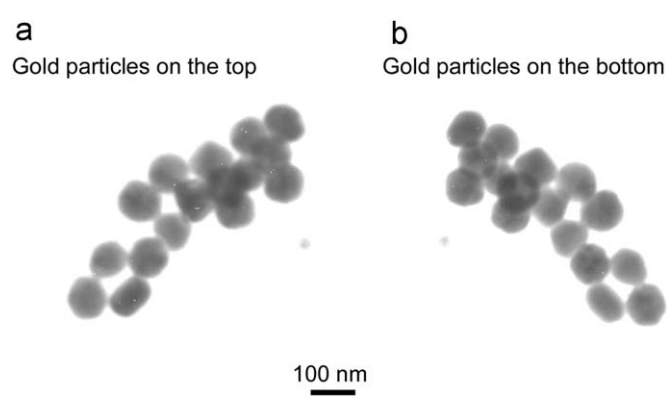

Fig. 8. Bright-field ultra-HVEM images of 100 nm gold particles on the: (a) top and (b) bottom surface of the 5 μm thick epoxy-resin specimen at the accelerating voltage of 2 MV.

top and bottom of the 15 μm thick specimen at the accelerating voltage of 2 and 1 MV in Fig. 9, we can see that image blurring, image contrast and the signal-to-noise ratio are all improved with the increase of accelerating voltage. As illustrated in Fig. 9a and b at the accelerating voltage of 2 MV, the diameter d of the gold particle on the top and bottom surface of the specimen is, respectively, ~29 and ~4 nm larger than its real size. In comparison, image blurring at 1 MV is ~59 and ~8 nm in Fig. 9c and d. The difference of image blurring between images of the gold particles on the top and bottom increases from ~25 nm at 2 MV to ~51 nm at 1 MV. Therefore, the top-bottom effect is shown to be more prominent with the decrease of accelerating voltage. Anyway, in our experiment, even for the gold particles on the top of the 15 μm thick specimen, the ultra-HVEM can reduce image blurring to ~0.2% of the specimen thickness at 2 MV. Here,

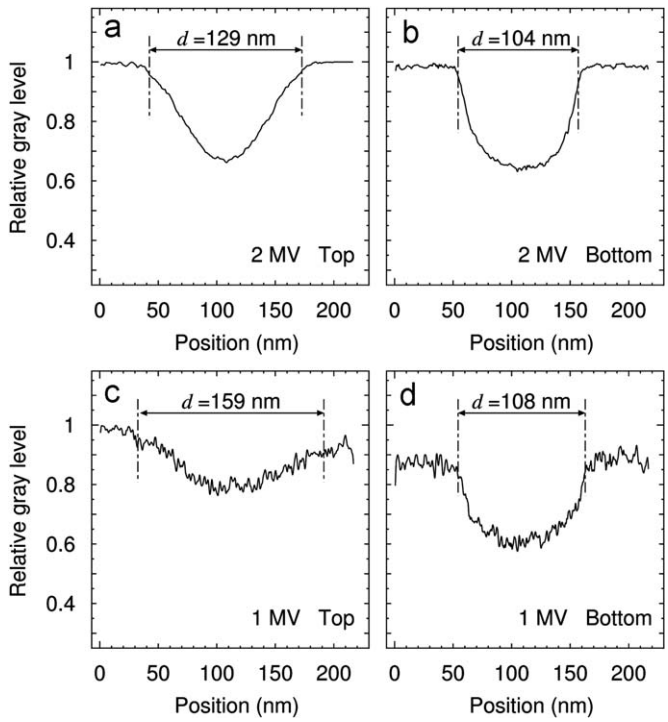

Fig. 9. One dimensional line profiles (average of 5 pixels) of the normalized gray level along the diameter direction from ultra-HVEM images of a 100 nm gold particle at different accelerating voltages of: (a), (b) 2 MV and (c), (d) 1 MV. The gold particle is, respectively, on the top and bottom surfaces of the 15 μm thick epoxy-resin specimens as shown in Fig. 7. The parameter d is the measured diameter of the 100 nm gold particle as the full width at tenth maximum. Image blurring can be estimated as ($d-100$ nm).

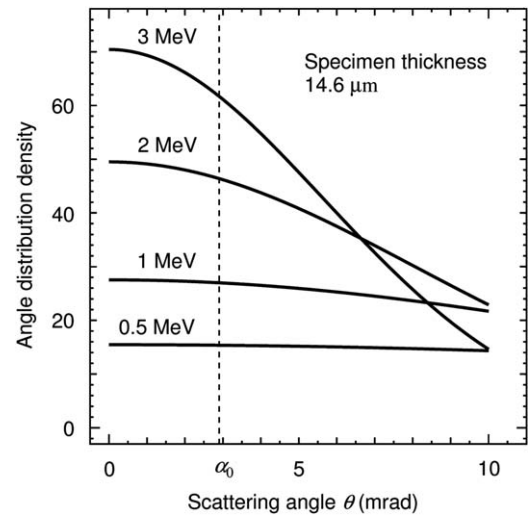

Fig. 10. Calculated normalized angular distributions of 0.5–3 MeV electrons passing a 70° tilted 5 μm thick epoxy-resin specimen with the effective thickness of 14.6 μm. As a half angle of the object aperture, the parameter α_0 is 2.92 mrad. Here, the higher electron energy makes the angular distribution of transmitted electrons more concentrated.

the image of the gold particles on the top of the specimen at 1 MV in Fig. 9c is blurred more significantly. However, gold particles on the bottom can be imaged with a higher quality at the accelerating voltage of 2 and 1 MV, as shown in Fig. 9b and d, respectively, although the deterioration of contrast to noise ratio [56] appears in the case of 1 MV for the decrease of electron transmission. On the other hand, the imaging quality of objects within a thick specimen should be between the results of the top and bottom conditions [48,57].

5. Analysis and discussion

We now turn to analyzing and discussing the effects of multiple elastic scattering on electron transmission and image blurring in above ultra-HVEM experiments. The properties of electron transmission are associated with the angular distribution of electrons by multiple elastic scattering in thick specimens. Fig. 10 depicts the normalized angular distributions $f(H,\theta)/\int_0^{\pi} f(H,\theta)d\theta$ calculated from Eq. (5) for the multiply scattered electrons of 0.5–3 MeV, which have passed the 14.6 μm thick epoxy-resin specimen. With the increase of electron energy, the partial elastic cross-section and the characteristic angle θ_0 of elastic scattering decrease according to Eq. (2), then the single elastic-scattering angle distributes in smaller angles [3], resulting in the decrease of the scattering angle of multiply elastically scattered electrons. The angular distribution of 3 MeV electrons is evidently narrower than that of 1 MeV not only for the decrease of scattering events but also for the reduction in scattering angles of one elastic-scattering event. It can be inferred that more intense signal of transmitted electrons can be obtained with the increase in accelerating voltage of electrons as shown in Fig. 6.

Furthermore, the exponential linear attenuation of electron transmission I_t/I_0 with specimen thickness H can exist in the regime of multiple elastic scattering, as seen in Fig. 5. In the case of 2 MeV electrons and the 2.92 mrad half angle α_0 of the objective aperture, calculations from $1-\sigma_{el}(\alpha_0)/\sigma_{el}$ according to Eqs. (1) and (2) show that about 52% of electrons in one elastic-scattering event have the scattering angle smaller than α_0, and thus a part of them may be scattered elastically a few times without being blocked by the objective aperture while passing a specimen thicker than the elastic mean free path. Therefore, the exponential linear attenuation valid for the single scattering range in which all scattered electrons are lost may be extended to the multiple-scattering regime, although the decay of I_t/I_0 in the exponential linear range is a little greater than that from 1 to e^{-1} over which the single scattering dominates. However, in the multiple elastic-scattering regime of the larger thickness, more electrons outside the objective aperture, i.e., in the range π–α_0, may return to α_0 by scattering because of a large number of scattering events and the wide angular distribution. As a result, the attenuation of $\log(I_t/I_0)$ will become more mild and deviate from linearity.

Multiple elastic scattering is also a dominant factor for image blurring and the top-bottom effect for thick specimens in our ultra-HVEM experiments. For 2 MeV electrons, the average elastic-scattering number n_{el} is about 20 for the 15 μm thick epoxy-resin specimen. After being scattered by a gold particle on the top of the specimen, the electrons will be spread laterally by multiple elastic scattering before exiting from the specimen. To extrapolate the trajectories to the top surface, a virtual gold-particle image is formed with more confusion [2,47]. The effect of the spatial broadening x_0 defined in Eq. (8) on image blurring will be more notable with the increase of specimen thickness H because of $x_0 \propto H^{3/2}$. The value of x_0 for 2 MeV electrons passing a 15 μm thick epoxy-resin specimen can be calculated as ~100 nm according to Eq. (8). Here, the calculated spatial broadening is apparently greater than real image blurring ~29 nm shown in Fig. 9a. This is because the small objective aperture can remove the electrons with scattering angles larger than its half angle [58].

However, the higher accelerating voltage can reduce the image quality degradation, due to the suppression of multiple elastic scattering, especially the decrease of elastic-scattering angles. When the accelerating voltage of electrons increases from 1 to 2 MV, image blurring for the gold particles on the top of the 15 μm thick epoxy-resin decreases about 2 times. This is basically consistent with the theoretical prediction of 1.8 times calculated with the spatial broadening defined in Eq. (8). Similarly, when the specimen thickness increases from 5 to 15 μm, image blurring for the top case increases about 6 times, compared with the increase of the spatial broadening of 5.2 times. Therefore, variations of image blurring with the accelerating voltage or the specimen thickness are consistent with those of the spatial broadening, indicating the dominant influence of multiple elastic scattering on image blurring for the top case.

The effect of multiple elastic scattering on image blurring should be distinguished from other resolution limits such as chromatic and spherical aberration. Chromatic aberration due to multiple inelastic scattering degrades image quality wherever objects are located in the thick specimen. Here, the chromatic aberration coefficient C_c of the ultra-HVEM is ~10 mm [24]. According to Eqs. (9) and (10), for images of the 15 μm thick epoxy-resin specimen observed at the accelerating voltage of 2 MV and the half angle α_0 of 2.08 mrad, we can calculate the width ΔE of the energy distribution of transmitted electrons and the point-to-point resolution r_c to be ~600 eV and ~5 nm, respectively. However, the corresponding point-to-point resolution [55] of the gold-particle image may be ~58 nm at least, a double value of measured image blurring of ~29 nm in Fig. 9a for the gold particles on the top surface, and therefore is much greater than r_c. Accordingly, chromatic aberration may be a minor factor in image blurring for this top case. On the other hand, the spherical aberration $C_s\alpha_0^3$ where the spherical aberration coefficient C_s is ~10 mm for the ultra-HVEM [24], is as small as ~0.9 Å in our case. Consequently, we believe that the spatial broadening within thick specimens by multiple elastic scattering is the main cause of image blurring for the gold particles on the top surface and therefore the top-bottom effect. Here, the origin of the top-bottom effect is different from that under thick specimens or high-resolution conditions in the conventional TEM. In the latter, inelastic scattering of electrons while passing the specimen may cause divergence of electrons and partially cover up the image information derived from elastic scattering [10,45–47].

On the other hand, when gold particles are located at the bottom of the thick specimen, image blurring is much smaller compared with the top case due to the absence of spatial broadening. Then, chromatic aberration becomes a relatively important cause of this weaker image blurring. The angular dispersion of electrons from multiple elastic scattering before reaching the gold particles on the bottom may be the other cause of image blurring of the relatively clear ultra-HVEM images shown in Fig. 7b and d. Moreover, the image quality for the bottom case can be improved at the higher accelerating voltage. In Fig. 9b and d, the increase of the accelerating voltage from 1 to 2 MV causes the decrease of ~4 nm in measured image blurring, which corresponds to the increase of ~8 nm at least in point-to-point resolution. Compared with the increase of ~5 nm in r_c from chromatic aberration, multiple elastic scattering may also contribute to the image quality degradation. Nevertheless, this effect is still difficult to confirm quantitatively since it may be affected by focusing and restriction of an objective aperture [55]. In addition, with the increase of specimen thickness or half angle of the objective aperture, the image quality for the bottom case has been observed to decrease slightly in our experiment. However, higher image contrast and brightness can be obtained at a larger objective aperture at the expense of a little resolution degradation. Here, we suggest that the significance of chromatic aberration and multiple elastic scattering to the image quality should be investigated more precisely.

Image blurring caused by multiple elastic scattering depends on both the specimen thickness and the electron energy. As illustrated in Eq. (8), the spatial broadening x_0 of electron beam causing image blurring for objects near the top of the thick specimen is proportional to $H^{3/2}/E^a$, in which H is the specimen thickness, E the electron energy, and $a<1$. Here, H will have a more obvious effect. Fig. 11 compares ultra-HVEM images of gold particles on the top of the 5 μm thick epoxy-resin specimen at 1 MV, 10 μm at 2 MV, and 14.6 μm at 3 MV, respectively, in which the specimen thickness and the accelerating voltage increase in an approximately equal scale. x_0 calculated for Fig. 11a–c are about 35, 54, and 67 nm. Here, image quality degrades successively. Therefore, for a very thick specimen, image deterioration due to the increase of specimen thickness will surpass the improvement from increasing the accelerating voltage in the same scale.

The variation of image contrast and the signal-to-noise ratio presented in the experiment can be explained from the electron scattering effect. Electron transmission decreases with the increase of specimen thickness due to more loss of elastically scattered electrons through the objective aperture. The decrease of brightness in background will be more than that in gold particle because epoxy-resin is much lighter than gold. Therefore, contrast of gold-particle images will be lowered. Moreover, noise in images becomes relatively prominent at lower background brightness and this will decrease the signal-to-noise ratio. Furthermore, increasing with the specimen thickness, inelastic scattering of electrons should degrade both image contrast and signal-to-noise ratio [59] as shown in Figs. 7a,b and 8a,b.

The accelerating voltage will affect image contrast and the signal-to-noise ratio as well. The increase of accelerating voltage from 1 to 2 MV can cause more increase in electron transmission for the epoxy-resin specimens than for the gold particles. Therefore, image contrast should be enhanced as shown in Fig. 7. However, if the accelerating voltage increases to be larger than 3 MV, the increase of electron transmission for the thick specimen should slow down and approach to saturation according to Eq. (7) where the angular parameter $\overline{\theta}$ defined with Eq. (6) is approximately inversely proportional to electron energy. It is inferred that image contrast may decrease. Anyway, noise in images becomes relatively small at higher background brightness, and therefore the signal-to-noise ratio increases. Moreover, the reduction in inelastic scattering at higher accelerating voltage will also contribute to the improvement of both image contrast and the signal-to-noise ratio. It is worth mentioning here that the increase of amplitude contrast observed with the ultra-HVEM in this work appears to be different from some other results in the conventional TEM. For example, the weak amplitude contrast for ice-embedded thin biological specimens was observed to decrease with the increase of accelerating voltage [60]. In this situation, the decrease of elastic cross-sections and scattering angles may further narrow the difference in electron transmission for light biological matter and ice with similar atomic weight [61]. Phase contrast for some coarse structures was also demonstrated to decrease with the increase of accelerating voltage [5].

Accordingly, the effect of multiple scattering on image quality can be decreased by increasing the MV accelerating voltage of electrons, and higher image quality and weaker top-bottom effect can therefore be obtained. For imaging very thick amorphous specimens, the ultra-HVEM should be superior to the conventional STEM whose accelerating voltage is usually lower than 300 kV because chromatic aberration can be considerably decreased at the MV accelerating voltage [19,62]. For example, compared with the obtainable image blurring of ~10 nm

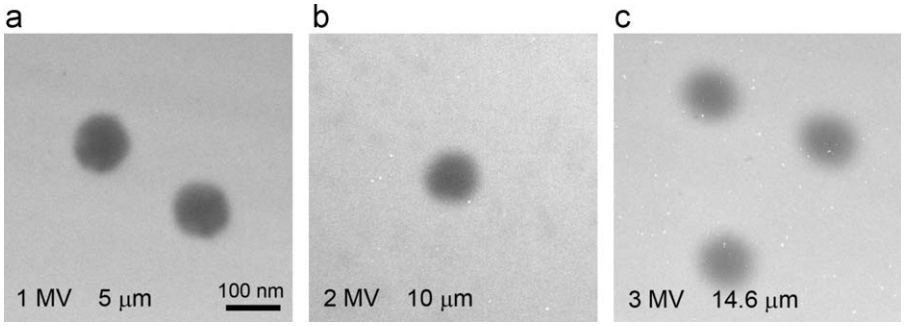

Fig. 11. Bright-field ultra-HVEM images of 100 nm gold particles on the top of the titled epoxy-resin specimens when the effective thickness of the specimens and the accelerating voltage increase with an approximate equal scale: (a) 5 μm and 1 MV; (b) 10 μm and 2 MV; (c) 14.6 μm and 3 MV.

reported for the gold particles on the top surface of a 6 μm thick specimen in a 300 kV STEM [35], the ultra-HVEM in this work can produce less image blurring of ~4 nm for imaging the gold particles on the bottom of the thicker specimen of 15 μm as shown in Fig. 9b. In fact, for specimens thicker than ~6 μm, resolution was shown to decrease more rapidly with the increase of specimen thickness in a 300 kV scanning confocal electron microscope [34]. Finally, image blurring due to multiple elastic scattering cannot be eliminated by means of energy filtering although an energy filter can improve image quality by removing some inelastically scattered electrons. Utilization of the higher MV accelerating voltage in TEM appears to be the better choice to improve image quality for microns-thick specimens.

6. Conclusions

By experiment and analysis, we have investigated the characteristics of multiple scattering of MeV electrons and its effects on electron transmission and imaging of microns-thick specimens in the bright-field TEM mode. The measurement and calculation results show that at the accelerating voltage of electrons from 0.5 to 3 MV, electron transmission I_t/I_0 for the microns-thick amorphous specimen and electron energy E follow the approximate power law as $I_t/I_0 \propto E^k$. Electron transmission for a 5 μm thick epoxy-resin specimen tilted to 70° (with the effective thickness of 14.6 μm) at the 3 MV accelerating voltage and was 7.2 times higher than that at 1 MV. The linear range for the logarithmic electron transmission and the effective thickness of the tilted epoxy-resin specimen was extended to the multiple scattering regime as ~4 μm at 2 MV. Moreover, with the increase in accelerating voltage from 1 to 2 MV, ultra-HVEM images were observed to be improved with less blurring, higher image contrast and signal-to-noise ratio, and the top-bottom effect decreased. The optimal images of 100 nm gold particles on the bottom of epoxy-resin more than ten microns thick have blurring of only several nanometers at 2 MV. These characteristics can be attributed to the reduction in both elastic and inelastic scattering in thick specimens, especially multiple elastic scattering. It is interesting to note that objects near the top surface of a very thick specimen can also be imaged more clearly by turning over the specimen, i.e., making objects near the bottom of the specimen. However, the effects of specimen thickness and accelerating voltage on image blurring were shown to be in different scales. The improvement on image quality by increasing the accelerating voltage would be limited by the same scale increase of specimen thickness. The experiment and analysis presented made us believe that the ultra-HVEM would be superior to the conventional STEM on the observation of very thick specimens because of the suppression of the spatial broadening of the electron beam at the MV accelerating voltage. The ultra-HVEM appears to be a more effective means on the observation or electron tomography of large-scale structures in microns-thick specimens. In further research, we will evaluate image quality for thick specimens quantitatively and clarify its formation due to multiple elastic scattering with a Monte-Carlo simulation under the condition of the ultra-HVEM.

Acknowledgments

We would like to thank Prof. Hirotaro Mori for encouragement and advice, and Dr. Kiyokazu Yoshida for assistance in experiments. This work was supported by the Specialized Research Fund for the Doctoral Program of Higher Education of China (Grant No. 20070698013) and by 'Nanotechnology Network Project of the Ministry of Education, Culture, Sports, Science and Technology (MEXT), Japan' at the Research Center for Ultrahigh Voltage Electron Microscopy, Osaka University (Handai multi-functional Nano-Foundry).

References

[1] A.V. Crewe, T. Groves, J. Appl. Phys. 45 (1974) 3662.
[2] T. Groves, Ultramicroscopy 1 (1975) 15.
[3] V.E. Cosslett, R.N. Thomas, Br. J. Appl. Phys. 15 (1964) 883.
[4] J. Frank, B.F. McEwen, M. Radermacher, J.N. Turner, C.L. Rieder, J. Electron Microsc. Tech. 6 (1987) 193.
[5] L. Reimer, in: Transmission Electron Microscopy, Springer-Verlag, Berlin, 1993.
[6] I. Angert, C. Burmester, C. Dinges, H. Rose, R.R. Schröder, Ultramicroscopy 63 (1996) 181.
[7] H.B. Zhang, F. Wang, A. Takaoka, J. Electron Microsc. 56 (2007) 51.
[8] R. McIntosh, D. Nicastro, D. Mastronarde, Trends Cell Biol. 15 (2005) 43.
[9] P. Ercius, M. Weyland, D.A. Muller, L.M. Gignac, Appl. Phys. Lett. 88 (2006) 243116.
[10] H. Hashimoto, J. Appl. Phys. 35 (1964) 277.
[11] A. Takaoka, T. Hasegawa, K. Yoshida, H. Mori, Ultramicroscopy 108 (2008) 230.
[12] J.C. Bouwer, M.R. Mackey, A. Lawrence, T.J. Deerinck, Y.Z. Jones, M. Terada, M.E. Martone, S. Peltier, M.H. Ellisman, J. Struct. Biol. 148 (2004) 297.
[13] K. Aoyama, T. Takagi, A. Hirase, A. Miyazawa, Ultramicroscopy 109 (2008) 70.
[14] Z.H. Levine, Appl. Phys. Lett. 82 (2003) 3943.
[15] Z.H. Levine, J. Appl. Phys. 97 (2005) 033101.
[16] P.A. Midgley, E.P.W. Ward, A.B. Hungria, J.M. Thomas, Chem. Soc. Rev. 36 (2007) 1477.
[17] B.F. McEwen, M. Radermacher, C.L. Rieder, J. Frank, Proc. Natl. Acad. Sci. USA 83 (1986) 9040.
[18] H.B. Zhang, C. Yang, A. Takaoka, J. Electron Microsc. 53 (2004) 617.
[19] H.B. Zhang, X.L. Zhang, Y. Wang, A. Takaoka, Rev. Sci. Instrum. 78 (2007) 013701.
[20] J. Frank, T. Wagenknecht, B.F. McEwen, M. Marko, C.E. Hsieh, C.A. Mannella, J. Struct. Biol. 138 (2002) 85.
[21] A.C. Van Dorsten, W.J. Oosterkamp, J.B. Le Poole, Philips Tech. Rev. 9 (1947) 193.
[22] G. Dupouy, J. Phys. D: Appl. Phys. 2 (1969) 769.
[23] S. Ozasa, Y. Kato, H. Todokoro, S. Kasai, S. Katagiri, H. Kimura, E. Sugata, K. Fukai, H. Fujita, K. Ura, J. Electron Microsc. 21 (1972) 109.
[24] A. Takaoka, K. Ura, H. Mori, T. Katsuta, I. Matsui, S. Hayashi, J. Electron Microsc. 46 (1997) 447.

[25] A.M. Glauert, J. Cell Biol. 63 (1974) 717.
[26] C.J. Wilson, D.N. Mastronarde, B.F. McEwen, J. Frank, Neuroimage 1 (1992) 11.
[27] M.E. Martone, T.J. Deerinck, N. Yamada, E. Bushong, M.H. Ellisman, J. Histotechnol. 23 (2000) 261.
[28] A.J. Gubbens, B. Kraus, O.L. Krivanek, P.E. Mooney, Ultramicroscopy 59 (1995) 255.
[29] J.G. Kim, J.H. Choi, J.M. Jeong, Y.M. Kim, I.H. Suh, J.P. Kim, Y.J. Kim, Bull. Korean Chem. Soc. 28 (2007) 391.
[30] K. Omoto, K. Tsuno, M. Ohsaki, S. Matsumura, Y. Tomokiyo, Micron 39 (2008) 666.
[31] H. Fujita, Proc. Jpn. Acad. Ser. B 81 (2005) 141.
[32] J. Loos, E. Sourty, K. Lu, B. Freitag, D. Tang, D. Wall, Nano Lett. 9 (2009) 1704.
[33] A.A. Sousa, M.F. Hohmann-Marriott, G. Zhang, R.D. Leapman, Ultramicroscopy 109 (2009) 213.
[34] N.J. Zaluzec, Microsc. Today 6 (2003) 8.
[35] A. Beorchia, L. Heliot, M. Menager, H. Kaplan, D. Ploton, J. Microsc. 170 (1993) 247.
[36] M.M. Mkrtchyan, J.A. Liddle, A.E. Novembre, W.K. Waskiewicz, G.P. Watson, L.R. Harriott, D.A. Muller, J. Vac. Sci. Technol. B 16 (1998) 3385.
[37] I. Pozsgai, Ultramicroscopy 107 (2007) 191.
[38] K. Maeyama, A. Takaoka, K. Ura, J. Electron Microsc. 43 (1994) 45.
[39] J.P. Martinez, J.L. Balladore, J. Trinquier, Ultramicroscopy 4 (1979) 211.
[40] G. Soum, F. Arnal, B. Jouffrey, P. Verdier, J. Microsc. Spect. Elec. 9 (1984) 419.
[41] J.K. Hyun, P. Ercius, D.A. Muller, Ultramicroscopy 109 (2008) 1.
[42] V. Morandi, P.G. Merli, J. Appl. Phys. 101 (2007) 114917.
[43] B.F. McEwen, A.B. Heagle, Int. J. Imag. Syst. Tech. 8 (1997) 175.
[44] S. Matsumura, K. Higashida, Tetsu to Hagane 94 (2008) 487.
[45] L. Reimer, P. Gentsch, Ultramicroscopy 1 (1975) 1.
[46] Y. Kamiya, H. Ishikawa, A. Ishikawa, J. Electron Microsc. 31 (1982) 210.
[47] L. Reimer, M. Ross-Messemer, Ultramicroscopy 21 (1987) 385.
[48] H.B. Zhang, C. Yang, A. Takaoka, Rev. Sci. Instrum. 76 (2005) 056106.
[49] H.B. Zhang, A. Takaoka, K. Miyauchi, Rev. Sci. Instrum. 69 (1998) 4008.
[50] D.C. Joy, in: Monte Carlo Modeling for Electron Microscopy and Microanalysis, Oxford University Press, New York, 1995.
[51] E. Zeitler, G.F. Bahr, Exp. Cell Res. 12 (1957) 44.
[52] J.M. Fernández-Varea, R. Mayol, J. Baró, F. Salvat, Nucl. Instrum. Meth. B. 73 (1993) 447.
[53] X. Sun, Z.J. Ding, Q.R. Pu, H.M. Li, Z.Q. Wu, W.Q. Gu, K.W. Peng, G.J. Wu, F.A. Zhang, N.K. Kang, J. Appl. Phys. 92 (2002) 3641.
[54] http://physics.nist.gov/PhysRefData/Star/Text/ESTAR.html.
[55] V.E. Cosslett, Z. Angew. Phys. 27 (1969) 138.
[56] P. Ercius, D.A. Muller, M. Weyland, L. Gignac, Microsc. Microanal. 13 (Suppl. 2) (2007) 824.
[57] C. Yang, H.B. Zhang, J.J. Li, A. Takaoka, J. Electron Microsc. 54 (2005) 367.
[58] R.F. Egerton, Ultramicroscopy 107 (2007) 575.
[59] K. Yonekura, M.B. Braunfeld, S. Maki-Yonekura, D.A. Agard, J. Struct. Biol. 156 (2006) 524.
[60] C. Toyoshima, K. Yonekura, H. Sasabe, Ultramicroscopy 48 (1993) 165.
[61] D.B. Williams, C.B. Carter, in: Transmission Electron Microscopy: Imaging III, Plenum Press, New York, 1996.
[62] S.P. Frigo, Z.H. Levine, N.J. Zaluzec, Appl. Phys. Lett. 81 (2002) 2112.